

Drift analysis in tilt-roll heliostats

Alejandro Martínez-Hernández, Iván B. Gonzalo, Manuel Romero, José González-Aguilar^{*}

High Temperature Processes Unit, IMDEA Energy, Avda. Ramón de la Sagra 3, 28935 Móstoles, Spain

ARTICLE INFO

Keywords:

Concentrated solar energy
Heliostat aiming
Tilt-roll
Drift
Ray-tracing

ABSTRACT

Drift is a relevant issue in concentrated solar tower facilities since this time-dependent pointing error severely affects their performance. This work deals with the optical analysis of drift for tilt-roll heliostats in terms of the geometrical parameters associated to the heliostat mechanical structure and the local time. For each drift source or error, flux maps have been obtained by means of Monte Carlo ray-tracing calculations as a function of the source magnitude and daily time in winter and summer solstices. Then the corresponding pointing errors and the drift curves are determined from the displacement of the center of gravity of the flux maps. As a result, drift related to each source is identified and characterized. Additionally, drift sources are compared in terms of the standard deviation and the mean of their daily pointing errors. The analysis evidences that main drift sources are the misalignments of the pedestal like the one of an inclination with respect to the zenith.

1. Introduction

Optical performance of concentrating solar towers or central receiver systems (CRS) relies on pointing accuracy of heliostats to re-direct and focus the sunlight onto the aiming points located into the area of the receiver (Romero et al., 2016). Pointing errors of heliostats may lead to dramatic changes in flux distribution on the target and directly affect the increment of power spillage around the aperture of the receiver. Heliostats are dual-axis sun-trackers with off-axis reflector optics where the pointing (or normal) vector bisects the angle between the sun-heliostat and heliostat-receiver vectors. Two orthogonal rotational axes, one commonly fixed over time and the other varying its orientation along the day, usually provide the dual-axis feature. Heliostats can be classified according to the orientation of the axes (Lipps and Vant-Hull, 1978; Mousazadeh et al., 2009; Chong and Wong, 2009) in azimuth-elevation, spinning-elevation, polar-oriented and tilt-roll. Large commercial heliostats are mainly azimuth-elevation type, also known as altitude-azimuth, in which the azimuth axis points at the zenith and the elevation axis is defined by the intersection of horizontal and facet planes (Guo et al., 2011; Guo et al., 2013a). Another type is the spinning-elevation, target aligned or receiver-oriented heliostat. This category has the spinning axis pointing at the target and the elevation axis is perpendicular to it (Chen et al., 2006; Guo et al., 2010). A great advantage of using this heliostat type is that the orientation of both the tangential and sagittal planes is always kept constant with respect to the reflector surface during tracking. This results in a partial astigmatism

compensation, thus improving the optical efficiency of the heliostat (Chen et al., 2004, 2006; Zaibel et al., 1995). However, this configuration requires an accurate installation and alignment (Larmuth et al., 2013). Finally, other heliostats are the polar-oriented and tilt-roll. In the polar-oriented, the fixed axis is parallel to the Earth's rotation axis, which results in an almost constant angular velocity of such axis (Chen et al., 2006, Torres-Roldán et al., 2015). Regarding the tilt-roll one, also named as fixed horizontal tracking mechanism, the tilt axis is fixed and contained in the horizontal plane. This type of heliostat allows an easy integration of linear actuators that provide a high potential of cost reduction of the drive mechanism for small-area heliostats in the range of few square meters and therefore improving the packing density of the solar field (Schramek and Mills, 2004; Larmuth et al., 2013). For instance, tilt-roll tracking-based heliostats were used in the concentrated solar tower (CST) facility located at IMDEA Energy Institute in Móstoles, Madrid (Spain), in which the authors claimed a packing density as high as 47% (Romero et al., 2019).

Irrespective of the drive system of the heliostat, major technical issues concern those related to accuracy and stability of heliostat pointing and particularly the deviation of the focused solar spot with respect to the aiming point along the day, known as drift (Díaz-Félix et al., 2014). Drift is due to pointing errors that depend on the time of the day, which could arise from many sources, as for example time delays, offsets and misalignments in the tracking structure (Díaz-Félix et al., 2014). Indeed, even for small angular errors, drift can be quite significant since the light beam usually travels a long distance from the heliostats to the receiver (slant range). Because of the drift, the performance of the CST facilities

^{*} Corresponding author.

E-mail address: jose.gonzalez@imdea.org (J. González-Aguilar).

<https://doi.org/10.1016/j.solener.2020.10.057>

Received 7 August 2020; Received in revised form 12 October 2020; Accepted 18 October 2020

Available online 28 October 2020

0038-092X/© 2020 The Authors. Published by Elsevier Ltd on behalf of International Solar Energy Society. This is an open access article under the CC BY license

(<http://creativecommons.org/licenses/by/4.0/>).

Nomenclature		Greek letters	
c	distance between tilt and roll axis	α	angle between pedestal projection on the horizontal plane and X-axis
l	distance between the roll axis and the facet	β	angle between pedestal and Z-axis
M_α	rotation matrix of α degrees around the Z-axis	γ	angle between tilt and east–west axes
M_β	rotation matrix of β degrees around the Y'-axis, with Y'-axis being the Y-axis rotated α degrees around the Z-axis	δ	rotation angle around the Z-axis of the target roll angle
M_γ	rotation matrix of γ degrees around the Z-axis	ε	roll angle
M_ε	rotation matrix of ε degrees around the roll axis	ε_0	roll angle set point
M_θ	rotation matrix of θ degrees around the Z-axis	η	angle between the facet plane and the roll axis
M_σ	rotation matrix of σ degrees around the tilt axis	θ	$\frac{\pi}{2}$ minus the angle between tilt and roll axes
\vec{n}	normal vector of the heliostat	σ	tilt angle
\vec{t}	normal vector to the target	σ_0	tilt angle set point
\vec{u}_s	unit sun vector	τ	time period between the solar time employed to solve the tracking equations and the actual solar time
\vec{u}_t	unit central ray vector		
\vec{u}_y	unit vector pointing to the South	Subscripts	
\vec{u}_z	unit vector pointing to the zenith	I	ideal
		RE	reference error
		PE	perpendicularity error
		PRE	pedestal rotation error
		PTE	pedestal tilt error
		CE	canting error

can be compromised as the radiative flux and the corresponding temperature distributions required could suffer variations over the day (Salomé et al., 2013).

In this context, the drift has received some attention in the literature, but mostly for heliostats with azimuth-elevation tracking system. One of the first studies on drift using this type of heliostats was carried out by Stone et al. (1998, 1999), in the Solar Two Power Tower Plant located near Barstow, California. In this study, the authors analyzed the drift curves for three sources of error, namely pedestal tilt, canting and reference errors, assuming a constant angular error of 1 mrad for each of them. More recently, Bonanos (2012) investigated numerically the drift due to the pedestal tilt, canting error and temporal delay for different angular errors of a heliostat located in a solar field in Pentakomo, Cyprus. For this study, a Monte-Carlo ray-tracing software, SolTrace (Wendelin, 2003), was used, instead of the commonly used central-ray approximation, in which only the ray coming from the center of the heliostat facet is considered to calculate the drift curves. Guo et al. derived a formula for azimuth-elevation tracking systems (Guo et al., 2011; Guo et al., 2013a), then using it to study the drift also for different errors of a heliostat located in Beijing (Guo et al., 2013b). In 2014,

Escobar-Toledo et al. analyzed the same three errors treated by Stone et al. (1999), but for the solar field located in Hermosillo, Mexico. Furthermore, the authors aimed to establish general qualitative rules about the drift behavior and studied the effect of the distance heliostat-target on the drift curves (Escobar-Toledo et al., 2014). In Iriarte-Cornejo et al., 2014, the authors proposed a dynamic compensation method to treat the simulated and experimental drift curves arising from different errors. In Lara-Cerecedo et al., 2016, the authors developed a tool to evaluate the flux distributions, including drift effects, based on analytical model by Collado et al. (1986). The authors followed this approach because of its advantage in computational speed in comparison to Monte Carlo ray-tracing methods. Recently, Carretero et al. (2019) developed a method that directly provides a relationship between the evolution of the drift curves and angular error values, employing reflective cylindrical surfaces.

This work aims at providing a deep understanding on the drift behavior in tilt-roll heliostats and thus covering the lack of information regarding this type of heliostats. The analysis makes use of Monte Carlo ray-tracing simulations to thoroughly investigate all the factors that could cause drift in tilt-roll tracking-based heliostats. The structure of

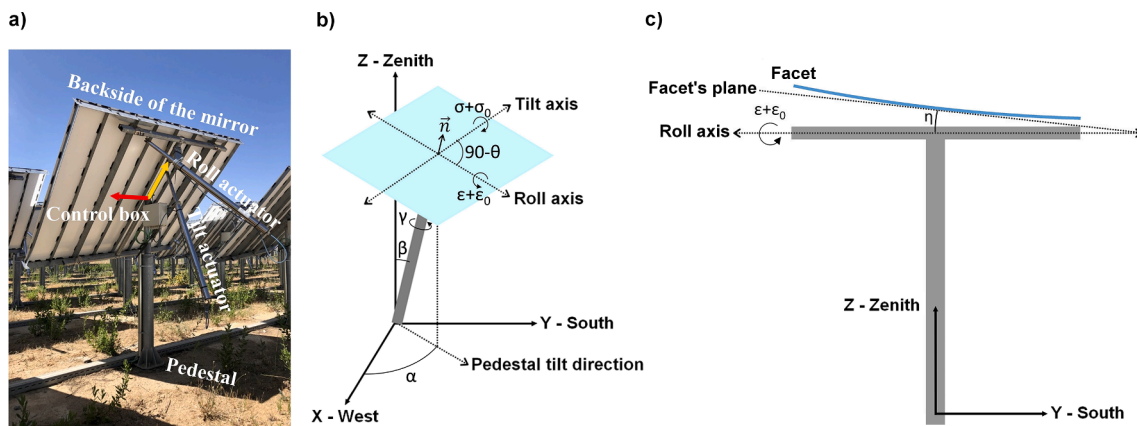


Fig. 1. (a) Tilt-roll heliostat in the VHCST facility (Northern Hemisphere). The tilt and roll axes are represented by arrows in red and yellow, respectively; (b) Drift sources due to angular misalignments (non-zero values of the angles σ_0 , ε_0 , θ , γ and β); and (c) Drift source due to non-ideal canting (non-zero value of the angle η). The direction of the black arrows in (b) and (c) indicates the direction of rotation for a positive angular deviation with respect to the ideal geometry.

Table 1
Parameters associated to each factor that causes drift.

Factors causing drift	Parameter	Value in an ideal heliostat
Reference error	ϵ_0 , roll angle set point; σ_0 , tilt angle set point.	$\epsilon_0 = 0^\circ$; $\sigma_0 = 0^\circ$
Perpendicularity error	θ , $\frac{\pi}{2}$ minus the angle between tilt and roll axes.	$\theta = 0^\circ$
Pedestal rotation	γ , angle between tilt and east–west axes.	$\gamma = 0^\circ$
Pedestal tilt	α , angle between pedestal projection on the horizontal plane and X-axis; β , angle between pedestal and Z-axis.	$\alpha = 0^\circ$; $\beta = 0^\circ$
Canting error	η , angle between the facet plane and the roll axis.	$\eta = 0^\circ$
Axes intersection error	c , distance between tilt and roll axes; l , distance between the roll axis and the facet.	$c = 0.077$ m; $l = 0.103$ m (for the VHCST)
Heliostat position error	δ , rotation angle around the Z-axis of the target.	$\delta = 0^\circ$
Time delay	τ , time period between the solar time employed to solve the tracking equations and the actual solar time.	$\tau = 0$ s

this paper is as follows. First, all the factors that could cause drift in this type of heliostats are described in detail. Then, the methodology employed for obtaining the drift curves for each of them is explained. Finally, the results are analyzed and a detailed discussion on the resulting drift of all the factors investigated is provided.

2. Factors causing drift

This section describes the factors that could cause drift in tilt-roll tracking-based heliostats. Fig. 1(a) shows a dual-axis heliostat belonging to the Very High Concentration Solar Tower (VHCST) facility located in Móstoles, Madrid, Spain (cf. Section 3) as example of this heliostat type (Romero et al., 2017, 2019; Batteiger et al., 2018). The tilt and roll axes are represented by red and yellow arrows, respectively. In an ideal heliostat (i.e. having no misalignments), the tilt axis is always fixed and parallel to the east–west axis, lying on the center of the heliostat, and orthogonal to the pedestal. The position of the roll axis depends on the position of the tilt axis and its horizontal projection is parallel to the north–south axis for the ideal heliostat. Fig. 1(b) and 1(c) display the factors causing drift, which are the angular misalignments, shown in Fig. 1(b) (non-zero values of the angles σ_0 , ϵ_0 , θ , γ and β), and the canting error shown in Fig. 1(c) (non-zero value of the angle η), all directly related to the heliostat structure.

By analyzing Fig. 1(b), the normal vector of the ideal heliostat, which has a perfect aligned structure, is given by $\vec{n}_I = M_\sigma M_\epsilon \vec{u}_z$, where M_σ is the rotation matrix around the tilt axis (X-axis), M_ϵ is the rotation matrix around the roll axis when the tilt angle is zero (Y-axis) and \vec{u}_z is the unit vector pointing to the zenith, i.e., the normal vector of the ideal heliostat facet in stow position.

$$M_\sigma = \begin{pmatrix} 1 & 0 & 0 \\ 0 & \cos\sigma & \sin\sigma \\ 0 & -\sin\sigma & \cos\sigma \end{pmatrix} \quad (1)$$

$$M_\epsilon = \begin{pmatrix} \cos\epsilon & 0 & \sin\epsilon \\ 0 & 1 & 0 \\ -\sin\epsilon & 0 & \cos\epsilon \end{pmatrix} \quad (2)$$

$$\vec{n}_I = (\sin\epsilon, \cos\epsilon\sin\sigma, \cos\epsilon\cos\sigma) \quad (3)$$

Any factor that modifies the variables in Eqs. (1)–(3) will eventually produce drift. This involves parameters linked to heliostat structure

(shown in Fig. 1), inaccurate local time, or heliostat position. All the causes of drift are summarized in Table 1 and will be described below.

2.1. Reference error

Reference error occurs when tilt and roll set points (ϵ_0 , σ_0) that establish the facet pointing at the zenith are not properly defined. The tilt and roll set points are obtained as minus the angle between the normal vector of the facet of the actual heliostat and the vertical direction and they are equal to zero in an ideal heliostat. The normal vector of the heliostat facet is generally given by:

$$\vec{n}_{RE} = (\sin(\epsilon + \epsilon_0), \cos(\epsilon + \epsilon_0)\sin(\sigma + \sigma_0), \cos(\epsilon + \epsilon_0)\cos(\sigma + \sigma_0)) \quad (4)$$

2.2. Perpendicularity error

The perpendicularity error appears when the tilt and roll axes are not orthogonal, and it is only determined by the manufacturing process of the heliostat. The perpendicularity error is described by the angle θ that indicates the deviation with respect to $\pi/2$. When this error is present, the roll axis is rotated θ degrees around the Z-axis and, as result, the normal vector of the heliostat is given by $\vec{n}_{PE} = M_\sigma M'_\epsilon \vec{u}_z$. In this expression, M'_ϵ is the rotation matrix around the roll axis after being rotated, i.e., M'_ϵ is the rotation matrix around the axis given by $M_\theta \vec{u}_y$, with M_θ being the rotation matrix around the Z-axis and \vec{u}_y being the unit vector pointing to the South.

$$M_\theta = \begin{pmatrix} \cos\theta & -\sin\theta & 0 \\ \sin\theta & \cos\theta & 0 \\ 0 & 0 & 1 \end{pmatrix} \quad (5)$$

$$M'_\epsilon = \begin{pmatrix} \cos\epsilon + (1 - \cos\epsilon)\sin^2\theta & -(1 - \cos\epsilon)\sin\theta\cos\theta & \sin\epsilon\cos\theta \\ -(1 - \cos\epsilon)\sin\theta\cos\theta & \cos\epsilon + (1 - \cos\epsilon)\cos^2\theta & \sin\epsilon\sin\theta \\ -\sin\epsilon\cos\theta & -\sin\epsilon\sin\theta & \cos\epsilon \end{pmatrix} \quad (6)$$

$$\vec{n}_{PE} = (\sin\epsilon\cos\theta, \cos\epsilon\sin\sigma + \sin\epsilon\cos\sigma\sin\theta, \cos\epsilon\cos\sigma - \sin\epsilon\sin\sigma\sin\theta) \quad (7)$$

2.3. Pedestal rotation error

When installing a heliostat in the field, its pedestal could be rotated thus resulting in a misalignment between the tilt and the east–west axes. This deviation is called pedestal rotation error and it is defined by the angle between both axes, γ . In a typical azimuth-elevation heliostat, this error could be corrected by applying an offset to the azimuth motor (Stone and Jones, 1999), but it cannot be corrected in a tilt-roll heliostat. When the pedestal is rotated, the normal vector is given by $\vec{n}_{PRE} = M_\gamma M_\sigma M_\epsilon \vec{u}_z$, where M_γ is the rotation matrix around the Z-axis, so $M_\gamma \equiv M_\theta$.

$$\vec{n}_{PRE} = (\sin\epsilon\cos\gamma - \cos\epsilon\sin\sigma\sin\gamma, \sin\epsilon\sin\gamma + \cos\epsilon\sin\sigma\cos\gamma, \cos\epsilon\cos\sigma) \quad (8)$$

2.4. Pedestal tilt error

Similarly to the pedestal rotation error, this error comes from a misalignment in the pedestal introduced when installing the heliostat in the field. Here the error is caused by a misalignment of the pedestal with the Z-axis. To evaluate this error and the resulting drift, two angles are required, α and β , as it is shown in Fig. 1(b), and referred as pedestal tilt direction and pedestal tilt, respectively. The first one is the angle between the X-axis and the pedestal projection on the XY- (or horizontal) plane and the second one is the angle between the pedestal and the Z-axis. When the pedestal is inclined, the normal vector is given by $\vec{n}_{PTE} = M_\beta M_\sigma M_\epsilon \vec{u}_z$, where M_β is the rotation matrix around the Y-axis, and this axis is calculated by rotating the Y-axis around the Z-axis α degrees, i.e., M_β is the rotation matrix around the axis given by $M_\alpha \vec{u}_y$. As

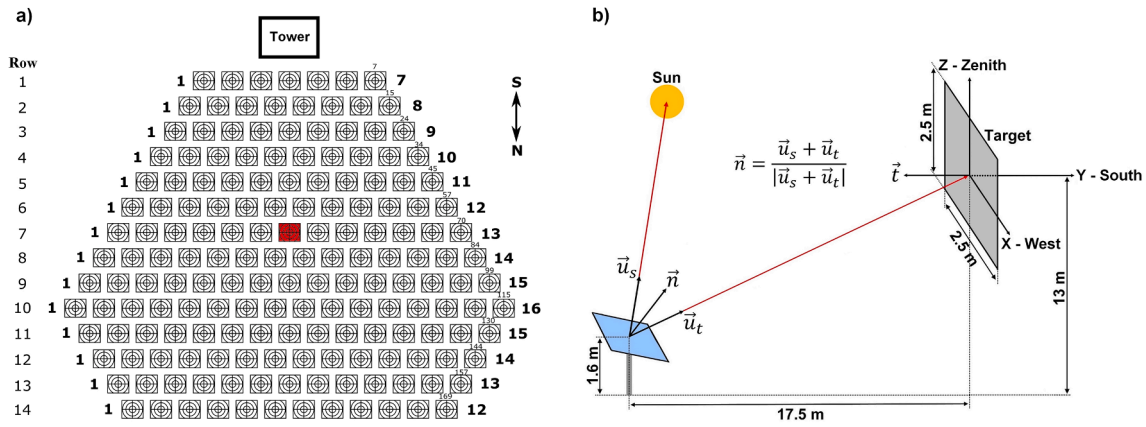


Fig. 2. (a) Heliostat field layout of the VHCST facility. The reference heliostat used as a test case is marked in red. (b) Model of the geometry of the problem for the heliostat under investigation shown in (a).

M_α is the rotation matrix around the Z-axis, then $M_\alpha \equiv M_\gamma \equiv M_\theta$.

$$M_\beta = \begin{pmatrix} \cos\beta + (1 - \cos\beta)\sin^2\alpha & -(1 - \cos\beta)\sin\alpha\cos\alpha & \sin\beta\cos\alpha \\ -(1 - \cos\beta)\sin\alpha\cos\alpha & \cos\beta + (1 - \cos\beta)\cos^2\alpha & \sin\beta\sin\alpha \\ -\sin\beta\cos\alpha & -\sin\beta\sin\alpha & \cos\beta \end{pmatrix} \quad (9)$$

$$\vec{n}_{PTE} = M_\beta \vec{n}_i \quad (10)$$

2.5. Canting error

The canting error arises when the optical axis of the heliostat facet is not perpendicular to the roll axis. This error can be characterized by the angle η between the facet plane and the roll axis (see Fig. 1(c)). It must be pointed out that the facet plane can be deviated in any other direction, but this deviation can always be decomposed into two, the one represented in Fig. 1(c) and another one perpendicular to it (Stone and Jones, 1999). Furthermore, it can be shown that this second deviation corresponds to a rotation around the roll axis, so this deviation will produce the same effect than a reference error in roll. When the facet undergoes a canting error as the one just described, the normal vector is given by $\vec{n}_{CE} = M_\sigma M_\eta M_\gamma \vec{u}_z$, where M_η is the rotation matrix around the X-axis, so $M_\eta \equiv M_\sigma$.

$$\vec{n}_{CE} = (\sin\cos\eta, \cos\sigma\sin\eta + \cos\sigma\sin\cos\eta, -\sin\sigma\sin\eta + \cos\sigma\cos\cos\eta) \quad (11)$$

2.6. Axes intersection error

In the ideal VHCST heliostat, there is a distance between both axes, c , and a distance between the roll axis and the center of the facet, l . Even though these distances can be considered in the tracking equations, a difference between the actual distances and those employed to solve the tracking equations will produce drift. When this error is present, the normal vector of the heliostat is the same as the normal vector given by Eq. (3). However, the point of application (i.e. the point where the origin of a vector is located) of the former varies with respect to the latter, which causes a drift.

2.7. Heliostat position error

It appears when the heliostat coordinates used for solving the tracking equations are different from the actual ones. If the orientation of the tilt and roll axes are the same for both heliostat coordinates, the normal vector will be the same and only its point of application will change due to the displacement of the pedestal. This is the same that happens with the axes intersection error. The difference with this error is

that, when the heliostat position changes, the vector defined by the points of application of the normal vector of the ideal heliostat and the normal vector of the shifted heliostat does not change along the day. This means that light is always reflected from the heliostat with the same direction as from the ideal heliostat and with the same relative orientation with respect to it. Therefore, this causes a pointing error constant along the day.

In order to be able to investigate this error in angular units instead of length units, the heliostat pedestal can be shifted from its original position in the field by applying a rotation around the Z-axis of the target given by an angle δ .

2.8. Time delay error

It comes from a shift between the solar time employed to solve the tracking equations and the actual solar time. In this case, the normal vector and its point of application are the same as the normal vector of the ideal heliostat given by Eq. (3). Nevertheless, due to the time delay, the relative orientation between the actual sun vector and the sun vector employed to orient the heliostat changes along the day, thus causing drift.

3. Simulation method

Selected heliostats of the VHCST facility located in Móstoles, Madrid, Spain (40.339 N, 3.880 W) are used in this analysis. This facility comprises 169 single-facet tilt-roll heliostats of 3 m² (1.6 m × 1.9 m) with focal lengths of 20 and 30 m (Romero et al., 2017, 2019). The reference heliostat is in the center of the solar field, corresponding to the seventh heliostat of the seventh row (7–7), and has a focal length of 20 m (Fig. 2 (a)).

To investigate the drift curves due to errors arising from misalignments in the heliostat, numerical flux maps are obtained through detailed Monte Carlo ray-tracing simulations. With the aim to attain the most general results, blocking and shadowing effects of the surrounding heliostats are not considered. For all the cases, flux maps are simulated, and the drift curves are determined using their centers of gravity. This approach provides a more detailed description of drift behavior with respect to reported studies where only the central ray was used (Guo et al., 2013b; Escobar-Toledo et al., 2014; Lara-Cerecedo et al., 2016). In fact, it leads to observe an intrinsic drift that appears even when there are no misalignments in the tracking system of the heliostat, which is not detected with the approximation of the central ray.

Numerical flux maps are obtained with a custom ray-tracing Matlab® code, which has been previously validated by comparing the simulation results with those obtained with the commercial ray-tracing software TracePro® (Gonzalo et al., 2020). The custom ray-tracing

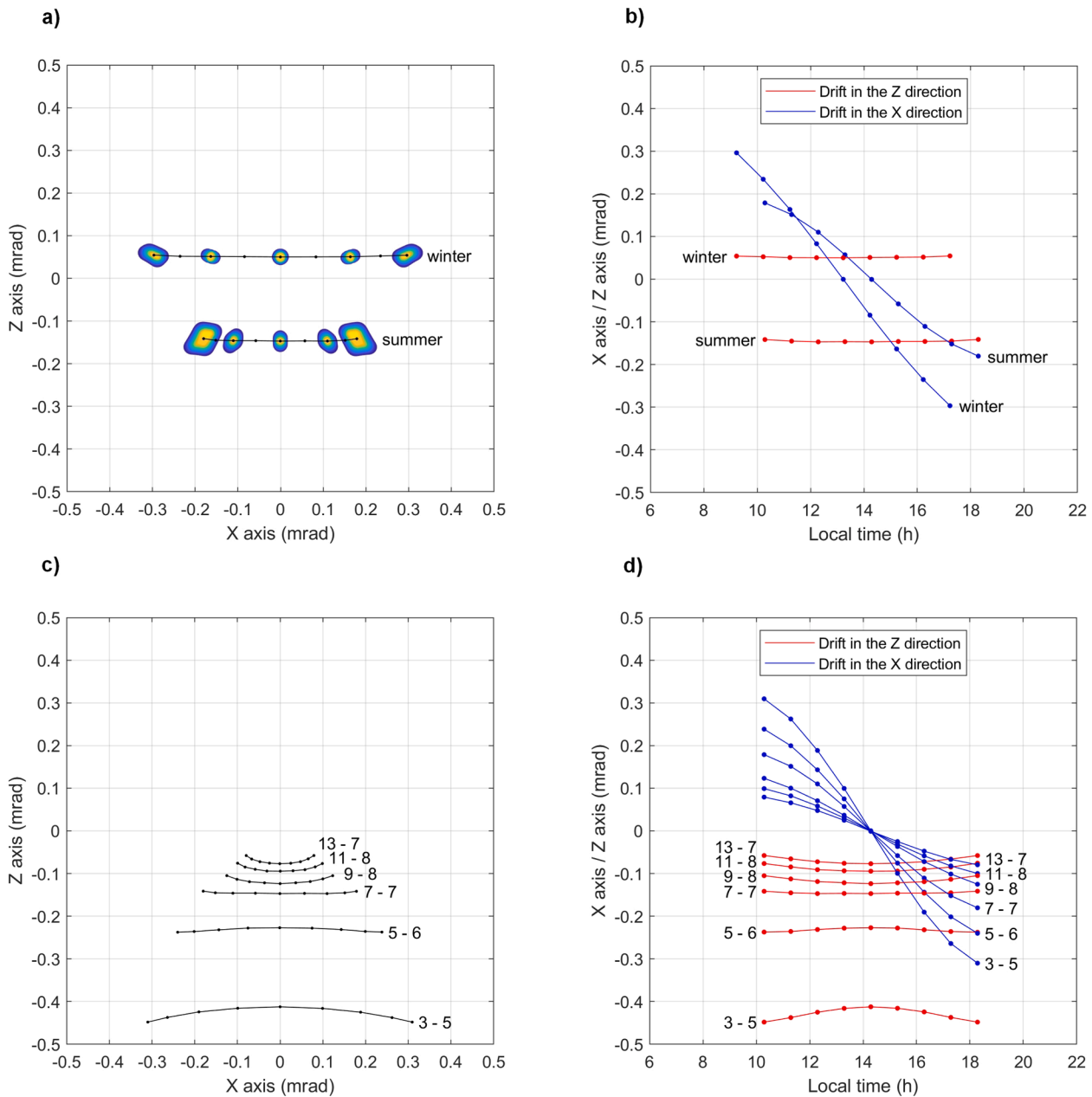


Fig. 3. (a) Intrinsic drift curves in summer and winter solstices for the reference heliostat (7–7). Flux maps simulated at ± 4 h, ± 2 h and 0 h with respect to the solar noon shown at a 1:300 scale. The position of the labels (summer/winter) indicates the beginning of the curve. (b) Drift in the X- (blue) and Z- (red) directions. Drift curves in summer and winter solstices are 1 h shifted because of the difference between summer and winter times. (c) Drift curves in summer solstice for heliostats situated along the north–south axis and in the center of its corresponding row. The heliostat closest to the target is the 3–5 (14.2 m) and the farthest the 13–7 (33.0 m). The position of the labels indicates the beginning of the curve. (d) Drift in the X- (blue) and Z- (red) directions.

program is particularly adapted to the VHCST geometry and similar configurations, so that it can perform simulations faster than TracePro®. This customized program works by firstly dividing the heliostat reflective surface into small elements and then tracing rays from each of them. For all the cases investigated here, simulations are performed tracing a bundle of 10,000 sunrays per reflecting element of the heliostat surface, with a total of 1,216 square reflecting elements of 5 cm side each. This results in 12.16 million of rays traced for the heliostat under investigation. In the simulations, the normal vector of every reflecting element is oriented according to the spherical curvature of the facet, therefore assuming that the heliostat facet is perfectly spherical. In addition, each sunray of the bundle is deflected from the main direction of the reflected sun vector according to a given limb-darkened sunshape distribution

(Romero et al., 2016). The sun vector is calculated employing the algorithm of Blanco-Muriel et al. (2001), which requires the latitude, longitude, local time, and date as input parameters. The 12.16 million of rays are traced over a square target of 2.5 m of side (Fig. 2(b)), which is located at 17.5 m to the south of the reference heliostat and at a vertical height of 13 m. These coordinates correspond to the actual target installed in the VHCST facility. The dimensions of the target guarantee that the incident flux is always completely impinging on its surface to rigorously evaluate the center of gravity.

Drift curves are usually calculated for each type of error described in Sec. 2 employing eight angular errors going from -20 mrad to 20 mrad in steps of 5 mrad (excluding 0 mrad). For the pedestal tilt error, these angular errors are applied to eight different tilt directions (0° , 45° , 90° ,

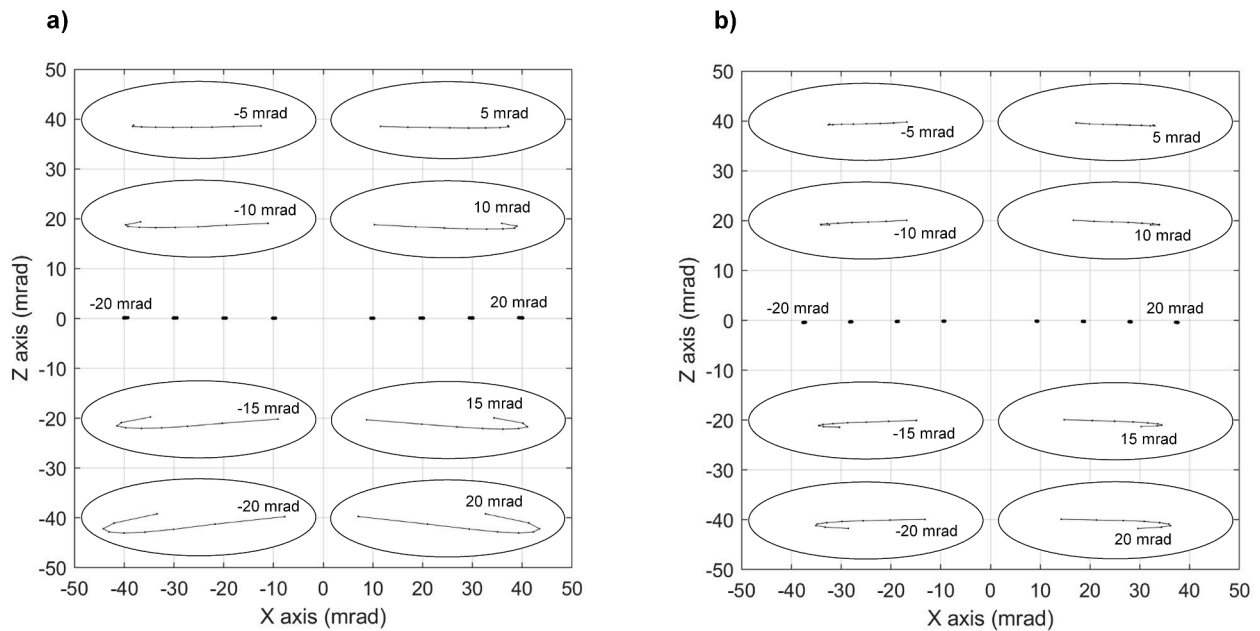


Fig. 4. Drift curves in (a) winter solstice and (b) summer solstice, when a reference error is present in roll. From left to right, the angular error goes from -20 mrad to 20 mrad. The curves have been zoomed-in 43 times inside the ellipses. The position of the label inside the ellipse indicates the beginning of the curve.

135° , 180° , 225° , 270° , and 315°). For the time delay error, these angular errors are converted in time delays considering that the sun rotates 360° every 24 h (Bonanos, 2012). As the axes intersection error cannot be expressed in angular units, variations in the length of the parameters c and l are introduced, instead, as a source of error. The drift curves are obtained simulating numerical flux maps every hour from 4 h before to 4 h after solar noon. This is done for summer and winter solstices. Finally, for each drift curve, the mean and the standard deviation of the pointing error of the daily 9 flux maps are evaluated, thus all the factors that cause drift can be quantitatively compared. Here, the pointing error is determined by the difference between the vectors going from the center of the facet to the center of the target and to the center of gravity of the calculated flux map and its components of the pointing

error are expressed as the angles subtended by the pointing error in the X and Z directions with respect to the center of the facet. Using this definition, the corresponding drift in terms of distances in the horizontal direction on the target is obtained multiplying the horizontal component of the pointing error, in angular units, by the heliostat-target distance (modulus of the vector going from the center of the facet to the center of the target). This distance is roughly $\sqrt{17.5^2 + (13.0 - 1.6)^2} = 20.89$ m for the reference heliostat (7–7), if the dependence on the parameters c and l is neglected (see Fig. 2 and Table 1). In turn, vertical drift on the target is obtained multiplying the vertical component of the pointing error, in angular units, by the heliostat-target distance and dividing by the cosine of the projection angle of the flux distribution

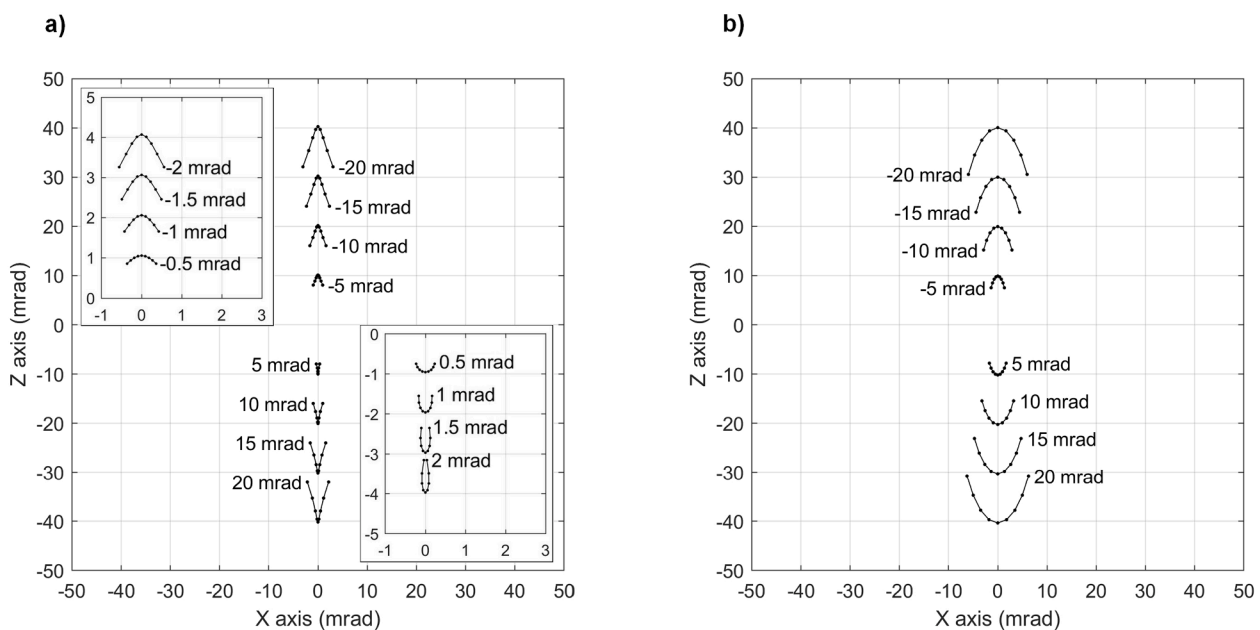


Fig. 5. Drift curves in (a) winter solstice and (b) summer solstice when a reference error is present in tilt. For winter solstice, drift curves are shown for angular errors below 5 mrad in absolute value. Each label indicates the angular error corresponding to each drift curve and its position indicates the beginning of the curve.

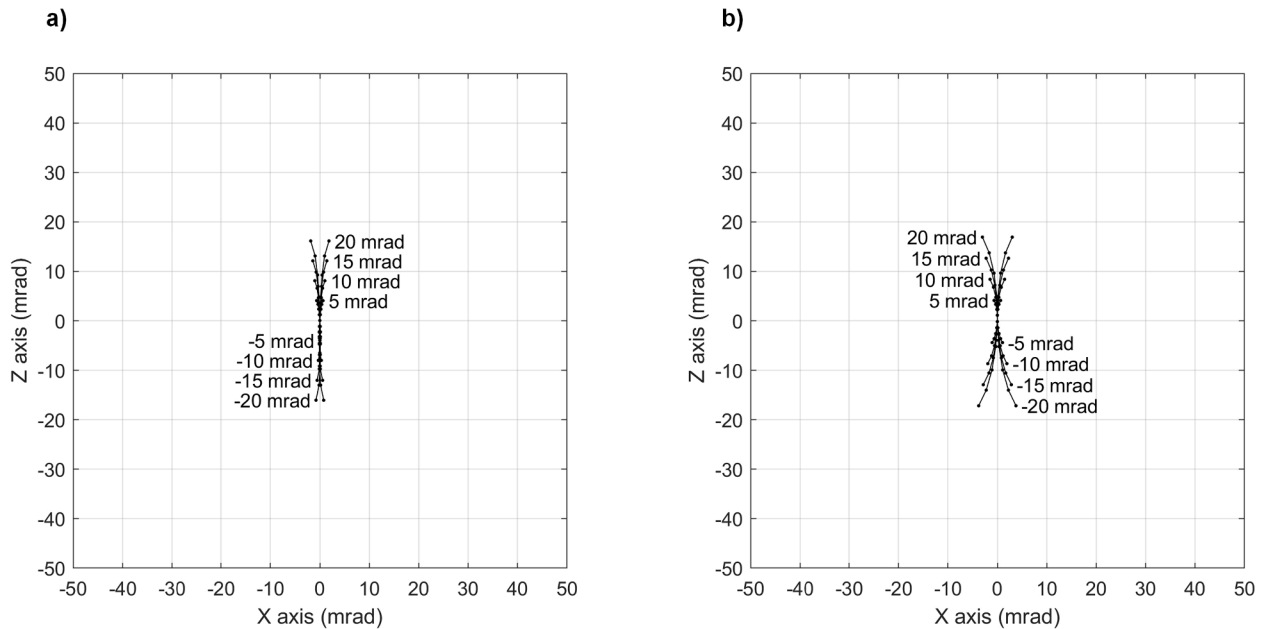


Fig. 6. Drift curves in (a) winter solstice and (b) summer solstice for a perpendicularity error between the tilt and roll axes. Each label indicates the angular error corresponding to each drift curve and its position indicates the beginning of the curve.

over the target (the angle between the normal vector to the target and the vector going from the center of the facet to the center of the target). This angle is roughly $\text{atan}((13.0 - 1.6)/17.5) = 33^\circ$ for the reference heliostat (7–7).

4. Results

4.1. Intrinsic drift

The intrinsic drift is associated to the fact that the incidence point of the central ray and the center of gravity of the flux map do not necessarily coincide (Escobar-Toledo et al., 2014). This situation, indeed, only occurs when the sun vector (\vec{u}_s), the central ray (\vec{u}_t), the normal vector of the heliostat (\vec{n}), and the normal vector to the target (\vec{t}) are collinear, which leads to a symmetric flux map with respect to the point where the central ray falls upon. The center of gravity of the flux map will depend on its shape. Since the flux map shape changes along the day due to astigmatism (Igel and Hughes, 1979), an intrinsic drift arises. Any other factor that modifies the shape of the flux map will slightly modify the drift curve produced by astigmatism. Factors affecting the flux map shape include the projection angle of the flux distribution over the target, the focal length of the heliostat, its slope error, the sun shape, etc.

The intrinsic drift obtained for the heliostat under study (Fig. 2(a)) is shown in Fig. 3(a) and (b) for summer and winter solstices. The drift is always smaller than 1 mrad in both the vertical (Z) and the horizontal (X) directions, which is less than those caused by other misalignments as it will be shown below. Furthermore, simulations of heliostats located in other positions in the field (Fig. 3(c) and (d)) show that the intrinsic drift decreases when the distance between the heliostat and the target increases. This is because heliostats located farther away from the target have a central ray more perpendicular to it, thus producing more symmetrical flux maps. These results agree with those reported in Escobar-Toledo et al., 2014. However, there the authors considered the intrinsic drift to be negligible and the investigation was conducted using only the central ray. As it will be shown, intrinsic drift has a strong influence when it is considered in the analysis involving other errors.

4.2. Reference errors

Fig. 4 shows the drift curves when there is a reference error in roll. As it can be seen, the extent of the drift curves in both X- and Z- axes is small for all the angular misalignments investigated here. In fact, it seems that there is no drift at all, only a constant pointing error that depends on the magnitude of the angular misalignment (ϵ_0). This pointing error can be explained by analyzing the movement of the roll axis. When the roll axis rotates, the orientation of the tilt axis is not modified, and thus the reflected light is deviated either towards the East ($X < 0$) or the West ($X > 0$) depending on the sign of the misalignment. It is worth to mention that this pointing error can be completely corrected by applying an offset to the roll motor of the same value and opposite sign as the reference error.

Fig. 5 displays the drift curves when there is a reference error in tilt. In this case, as the movement of the tilt axis modifies the orientation of the roll axis, a more pronounced drift is obtained. Fig. 5(a) and (b) show that the drift curves have a similar shape in both winter and summer, but the direction is inverted. Thus, when the angular errors are negative, the center of gravity moves along the day from west ($X > 0$) to east ($X < 0$) for winter solstice and from east to west for summer solstice. Furthermore, the effect of the intrinsic drift can be clearly noticed in these curves, especially in those corresponding to winter solstice. As shown in Fig. 3, the intrinsic drift results in the center of gravity moving from west to east. Now, looking at the drift curves for winter solstice, shown in Fig. 5(a), it is observed that when the center of gravity moves in the same direction of that corresponding to the intrinsic drift (negative angular errors), the drift curves are more opened than those having the opposite direction (positive angular errors). This is because all the drift curves shown in Fig. 5 are indeed affected by the intrinsic drift, and therefore there is a convolution between this one and the drift due to the reference error in tilt. To clearly show this phenomenon, drift curves have been simulated for rotation angles below 5 mrad in absolute value for winter solstice, and the results are shown in the zoom-in of Fig. 5(a). We observe that for positive angular errors, the drift direction gets inverted while decreasing the angular error, resembling more the one associated to the intrinsic drift shown in Fig. 3(a). Finally, it is worth to remark that this drift can be completely corrected by applying an offset to the tilt motor of the same value and opposite sign as the reference error, similarly to the case of the reference error in roll.

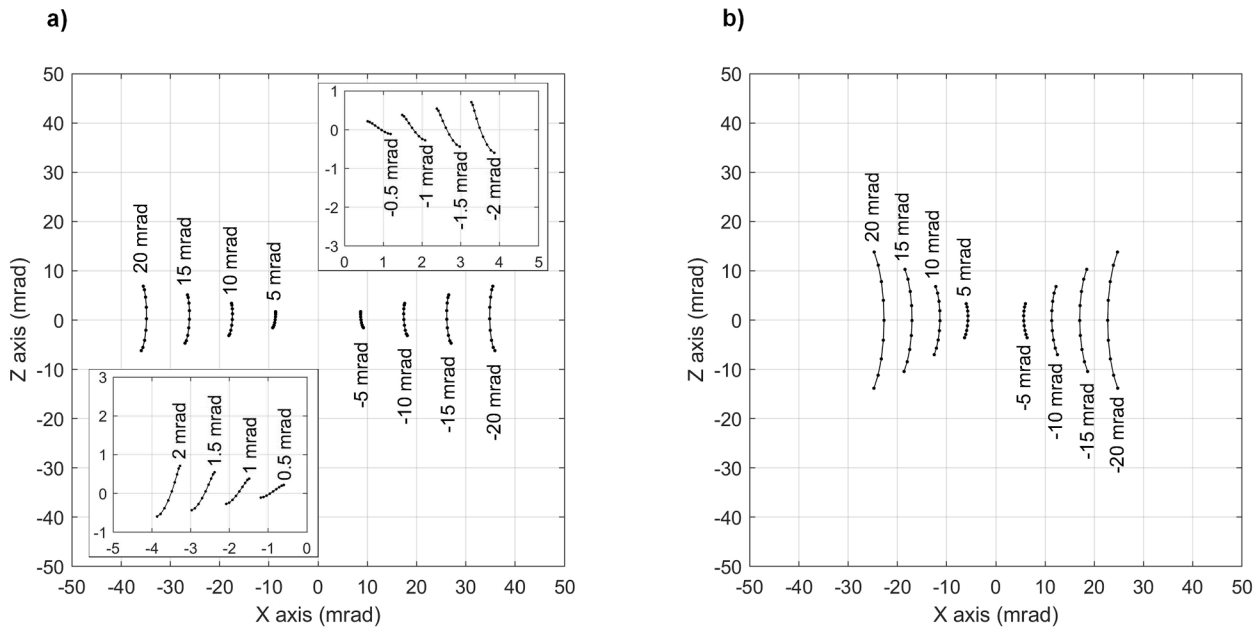


Fig. 7. Drift curves in (a) winter solstice and (b) summer solstice when the pedestal is rotated. For winter solstice, drift curves are shown for angular errors below 5 mrad in absolute value. Each label indicates the angular error corresponding to each drift curve and its position indicates the beginning of the curve.

4.3. Perpendicularity error

The drift curves produced by the perpendicularity error are shown in Fig. 6. They are almost vertical lines, in which the direction of the movement of the center of gravity along the day is determined by the direction of rotation of the roll axis around the Z-axis. Therefore, the drift goes from top ($Z > 0$) to bottom ($Z < 0$) when the angular error is positive. In addition, an interesting feature of this source of drift is that the pointing error of all the curves is zero at solar noon. This can be explained by the fact that at solar noon, the sun, the heliostat, and the center of the target are contained in the vertical plane defined by $X = 0$. This means that the roll angle (ϵ) is zero and therefore, even if both roll and tilt axes are not perpendicular ($\theta \neq 0$), the normal vector in Eq. (7) is the same as the normal vector of the ideal heliostat given by Eq. (3). Note that the pointing error will always be zero for any heliostat in the field whenever the roll angle is zero.

4.4. Pedestal rotation

When the pedestal is rotated, the reflected light is deflected on the target either to the East ($X < 0$) or to the West ($X > 0$) depending on the direction of the rotation, given by the sign of gamma, as shown in Fig. 7. Furthermore, the resulting drift is mainly vertical, and its direction also depends on sign of gamma. Thus, a positive rotation of the pedestal ($\gamma > 0$) results in a drift going from top ($Z > 0$) to bottom ($Z < 0$) and vice versa. Additionally, intrinsic drift has also an influence here. Looking at Fig. 7, it is observed that the smaller the rotation of the pedestal, the larger the relative displacement of the curve from west to east. For a deepest study of this phenomenon, drift curves have been simulated for rotation angles below 5 mrad in absolute value for winter solstice, and the results are displayed in the zoom-in of Fig. 7(a). These results pointed out that by decreasing the rotation angle, the drift direction changes from vertical to almost horizontal, resembling more the one associated to the intrinsic drift shown in Fig. 3(a).

4.5. Pedestal tilt

Two angles are required for evaluating this drift, α and β , where α denotes the tilt direction and β the tilt angle. For the study of this error,

eight different tilt directions have been chosen: west, southwest, south, southeast, east, northeast, north and northwest, corresponding to α values of $0^\circ, 45^\circ, 90^\circ, 135^\circ, 180^\circ, 225^\circ, 270^\circ,$ and 315° , respectively. Then, for each direction, drift curves have been calculated only for the 4 positive values of the tilt angle β : 5, 10, 15 and 20 mrad. The reason to use only the positive values of β is that the negative values produce the same drift curves than the positive values of β with the opposite tilt direction. This can be seen in Fig. 1(b), where the pedestal tilt will be the same for $\alpha = \alpha_0$ and $\beta = \beta_0$ than for $\alpha = \alpha_0 + 180^\circ$ and $\beta = -\beta_0$. We can demonstrate this result by introducing both values of α and β in Eq. (9), which results in the same rotation matrix and therefore the same drift.

Fig. 8 shows the drift curves for north, south, east, and west tilt directions. When the pedestal is tilted along the east–west axis, shown in Fig. 8(a) and (b), the reflected light is deflected on the target towards the East (West) corresponding to the tilt to the East (West) direction. In this way, the set of drift curves located in the East (West) correspond to a pedestal tilt to the East (West). These drift curves are mainly vertical and their direction depends on the tilt direction, i.e., from bottom ($Z < 0$) to top ($Z > 0$) for a pedestal tilted to the East, and the opposite for a pedestal tilted to the West. This general behavior of the drift curves is like that of the pedestal rotation error, the only difference is their curvature, convex in one case and concave in the other. On the other hand, when the pedestal is tilted along the north–south axis, the drift curves are similar to the drift curves due to a reference error of the tilt motor. This is because both errors produce the same misalignment of the roll axis, so the same normal vector is obtained in both cases. Even though the normal vector is the same, the point of application of the normal vector is slightly different depending on the error, which produces a shift of the drift curve. In fact, this shift can be noticed by comparing the drift curves in Fig. 5 with those in Fig. 8(c) and (d). When the pedestal is tilted towards the South, the drift curves are slightly shifted to the bottom part of the target, and when the pedestal is tilted towards the North, the drift curves are slightly shifted to the top part. While not shown here, when the pedestal is tilted along the southwest–northeast axis or along the southeast–northwest axis, the drift curves are a convolution of the corresponding drift curves of Fig. 8. Finally, it is also worth to remark that again the effect of the intrinsic drift can be clearly noticed in all the drift curves.

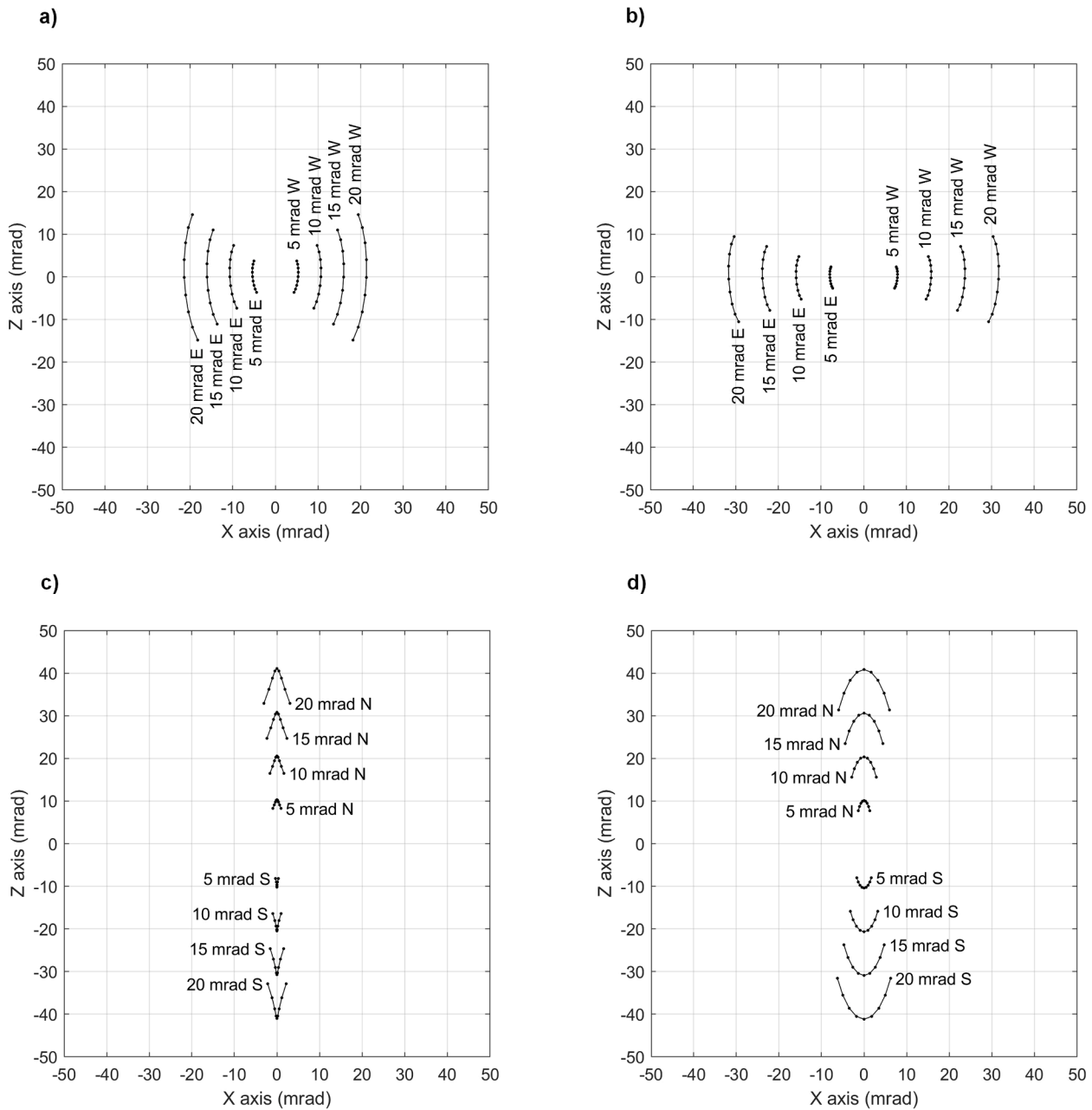


Fig. 8. Drift curves in (a, c) winter solstice and (b, d) summer solstice, when the pedestal is tilted. Each label indicates the tilt angle and the direction (W, west; S, south; E, east; N, north) corresponding to each drift curve. Its position indicates the beginning of the curve.

4.6. Canting error

Fig. 9 shows the drift curves when the facets undergo a canting error as shown in Fig. 1(c). These curves are similar to those corresponding to the reference error in tilt (Fig. 5) and to those corresponding to the pedestal tilt along the north–south axis (Fig. 8(c) and (d)). As explained above, these two errors produce the same misalignment of the roll axis, which results in the same normal vector and drift curves in both cases. However, the canting error does not produce any misalignment on the roll axis, and only when the roll angle is zero, the same normal vector is obtained in all the three cases. Therefore, for small roll angles, the normal vector given by the canting error is close to the normal vector produced by the other two, thus producing similar drift curves. Consequently, this error could be partially corrected by only applying an offset to the tilt motor.

4.7. Axes intersection error

This error cannot be expressed in angular units, because it depends on the distance between the center of both axes, c , and the distance between the center of the roll axis and the center of the facet, l . The nominal values for distances c and l are set to 0.077 m and 0.103 m, respectively, and they correspond to mean values measured in the VHCST solar facility.

Maintaining constant the distance l , four drift curves have been calculated by solving the tracking equations with the next four c -values: $c_1 = 0$, $c_2 = 2c$, $c_3 = 4c$ and $c_4 = 8c$. In the same way, maintaining constant the nominal value of c , four drift curves have been calculated for the next four l -values: $l_1 = 0$, $l_2 = 2l$, $l_3 = 4l$ and $l_4 = 8l$. Fig. 10 illustrates the drift curves obtained. It is observed that when the c parameter varies, corresponding to Fig. 10(a) and (b) in winter and summer solstices, respectively, the drift obtained is small and it seems

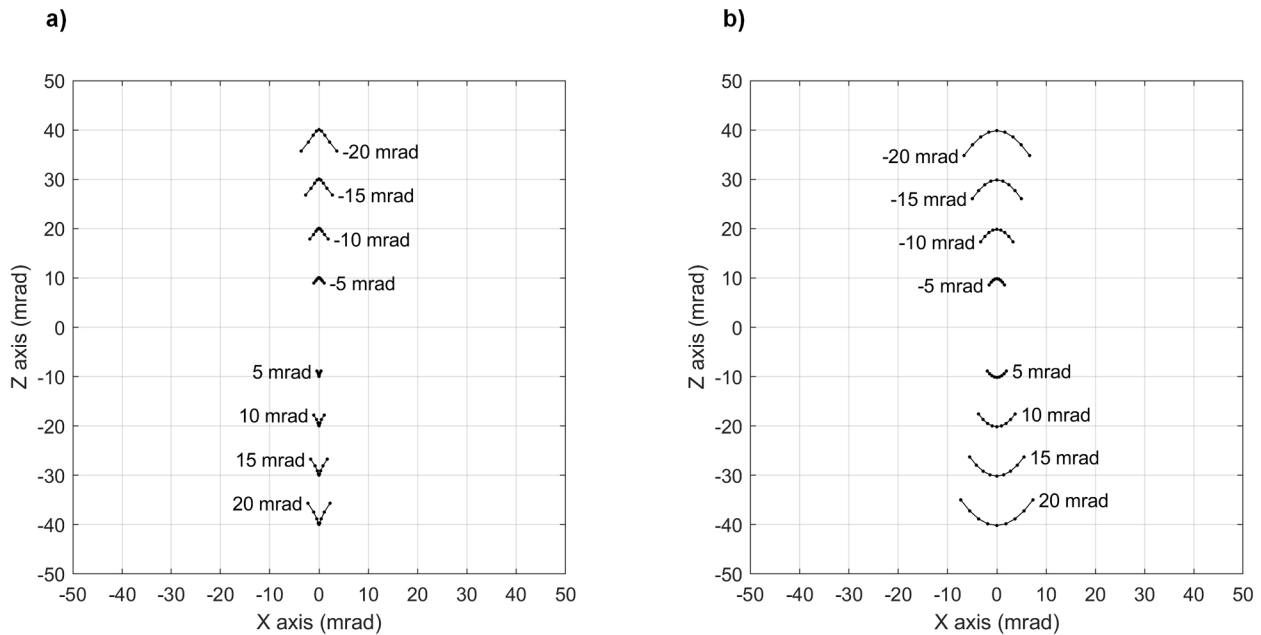


Fig. 9. Drift curves in (a) winter solstice and (b) summer solstice, when the facet has a canting error. Each label indicates the angular error corresponding to each drift curve and its position indicates the beginning of the curve.

that there is only a constant pointing error. Furthermore, this pointing error due to the variation of c at constant l is small. In contrast, the drift curves obtained by varying l at constant c are significant. In any case, the drift by axes intersection error could be dismissed since it requires variations in c and l parameters >100% of their nominal value to obtain significant drift curves. Such as large variations are unexpected in practice.

4.8. Heliostat positioning error

In order to investigate this error, the tracking equations have been solved assuming that the heliostat is located in the position $(x, y, z) = (0 \text{ m}, -17.5 \text{ m}, 0 \text{ m})$, but in fact it is located in the positions given by Table 2. These positions are calculated by applying a rotation around the Z-axis of the target given by the angle δ , as explained in Sec. 2. These rotations mainly produce a displacement of the heliostat along the east–west axis, and the reflected light is deflected on the target towards to the East ($X < 0$) or West ($X > 0$) according to the displacement direction. Fig. 11 shows the drift curves obtained. As explained in Sec. 2, the pointing error due to an error in the position of the heliostat in the field is constant along the day, which results in drift curves only given by the intrinsic drift. However, the drift curves are shifted with respect to those in Fig. 3.

4.9. Time delay

With the aim to investigate this error in angular units instead of temporal units, we can consider that the sun rotates 360° every 24 h, meaning that the sun takes 13.75 s to rotate 1 mrad (Bonanos, 2012). Thus, the eight angular errors used here correspond to the following temporal delays, τ : -275 s , -206.25 s , -137.5 s , -68.75 s , 68.75 s , 137.5 s , 206.25 s , and 275 s . If the delay is positive, the actual solar time is ahead with respect to the time employed to solve the tracking equations. Fig. 12 shows the drift curves obtained for the eight different angular errors. It is observed that the drift is more pronounced in winter than in summer for the same angular error. Nevertheless, time delays higher than 60 s are needed to produce a significant drift, which is a long temporal delay, not expected in practice.

5. Discussion

This section presents an assessment of all the drift errors to identify those with higher impact on heliostat drift. The mean and the standard deviation of the X- and Z- components of the pointing error are used for this comparison and calculated as (Escobar-Toledo et al., 2014).

$$\mu_x = \frac{1}{N} \sum_{i=1}^N X_i \tag{12}$$

$$\mu_z = \frac{1}{N} \sum_{i=1}^N Z_i \tag{13}$$

$$\sigma_x = \sqrt{\frac{1}{N-1} \sum_{i=1}^N (X_i - \mu_x)^2} \tag{14}$$

$$\sigma_z = \sqrt{\frac{1}{N-1} \sum_{i=1}^N (Z_i - \mu_z)^2} \tag{15}$$

where $N = 9$ is the number of points of the drift curves, and X_i and Z_i are the X and Z components of the pointing error of the point i , respectively. The standard deviation is associated to the extent of the drift curve, while the mean is related to the displacement (positive or negative) of the curve with respect to the center of the target in both X or Z directions. Table 3 shows the mean and the standard deviation of the drift curves evaluated with an angular error of 20 mrad (1.15°) for all the factors causing drift except for the axes intersection error. This one is excluded because there is not a direct transformation between the angular units and the parameters (c and l) used for its characterization. Moreover, for the error due to the pedestal tilt only drifts curves corresponding to tilts towards the East and the South are considered. Tilts towards the West and the North and angular errors of -20 mrad are discarded because it gives almost the same information. Additionally, and for reference, the mean and the standard deviation of the intrinsic drift are shown in Table 4.

In general, the most significant drift source will be that one with the largest extent, i.e. with the largest standard deviation. Furthermore,

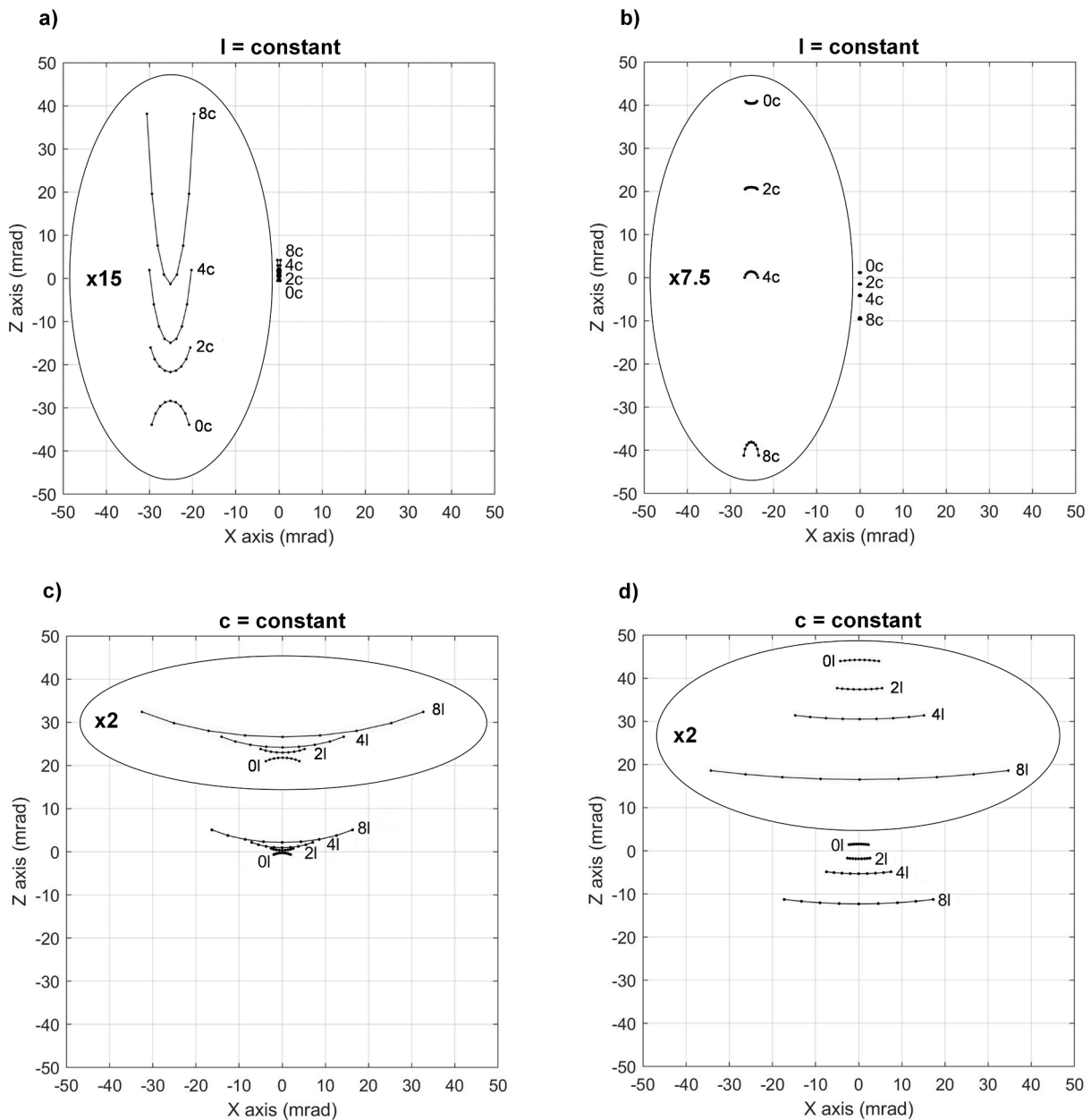


Fig. 10. Drift curves in (a, c) winter solstice and (b, d) summer solstice for several values of c and l distances. The curves have been zoomed-in inside the ellipses and the magnification factor is indicated inside. Each label indicates the length of the parameter corresponding to each drift curve. Its position indicates the beginning of the curve.

Table 2

Position of the heliostat (x and y coordinates) after a rotation around the Z -axis of the target. Note that X positive (negative) means that the position of the heliostat is shifted to the West (East).

δ (mrad)	-20	-15	-10	-5	5	10	15	20
x-coordinate (m)	-0.350	-0.262	-0.175	-0.087	0.087	0.175	0.262	0.350
y-coordinate (m)	-17.497	-17.498	-17.499	-17.500	-17.500	-17.499	-17.498	-17.497

when two drift factors reach similar standard deviation, the most important drift source will be the one with the largest separation from the center of the target, that is, with the largest mean. On the other hand, a drift factor with a non-zero mean can partially be corrected and move toward the center of the target by mean of two methods. The first one is applicable for any drift source and consists on modifying the aiming point of the heliostat to center its flux map on the target at solar noon. This leads to displace the drift curve without significantly altering its

shape (Escobar-Toledo et al., 2014). Second procedure lies to apply a constant offset to the roll motor, but it is only valid when the drift curve can be effectively centered by actuating over this motor. This is because a reference error in roll produces drift curves with a small standard deviation. Therefore, if the curve can be centered by actuating over the roll motor, the resulting drift curve will have almost the same shape than the original one. This second method is appropriate for the drift sources of which mean in the Z - direction are close to zero, such as the

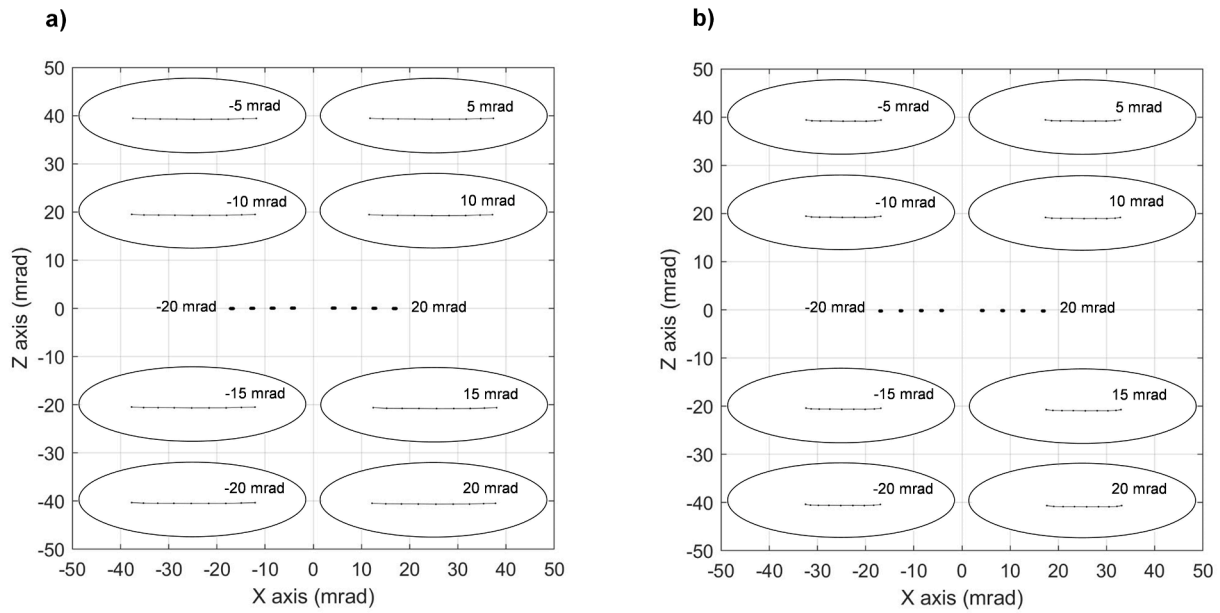


Fig. 11. Drift curves in (a) winter solstice and (b) summer solstice when the heliostat has an error in its position in the field. From left to right, the angular error goes from -20 mrad to 20 mrad. The curves have been zoomed-in 43 times inside the ellipses. The position of the label inside the ellipse indicates the beginning of the curve.

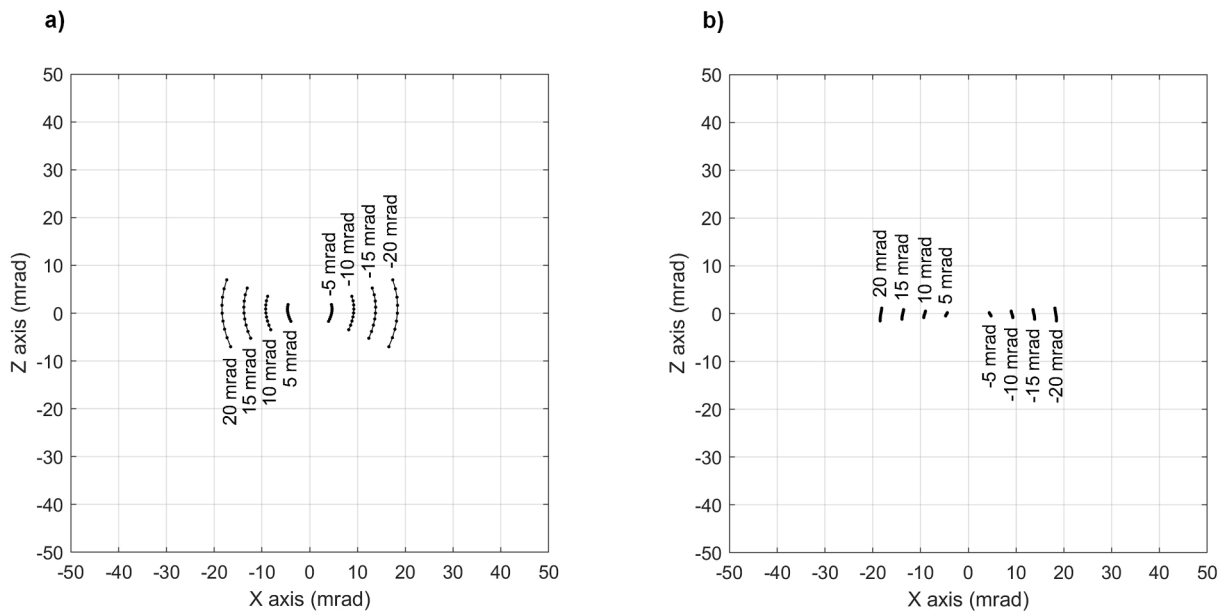


Fig. 12. Drift curves in (a) winter solstice and (b) summer solstice when there is a temporal delay. Each label indicates the angular error corresponding to each drift curve and its position indicates the beginning of the curve.

Table 3

Mean and standard deviation of the drift curves obtained for an angular error of 20 mrad for the factors causing drift.

Drift error	Winter solstice				Summer solstice			
	μ_x (mrad)	σ_x (mrad)	μ_z (mrad)	σ_z (mrad)	μ_x (mrad)	σ_x (mrad)	μ_z (mrad)	σ_z (mrad)
Reference in roll	39.9	0.3	0.1	0.0	37.5	0.2	-0.4	0.0
Reference in tilt	0.0	1.3	-36.6	3.1	0.0	4.4	-36.2	3.7
Tilt-roll axes perpendicularity	0.5	0.6	0.1	11.6	-1.4	1.3	-0.1	12.3
Pedestal rotation	-35.3	0.4	0.3	5.0	-23.6	0.8	0.0	9.9
Pedestal tilt - East	-20.3	1.1	-0.1	10.4	-30.9	0.8	-0.5	7.3
Pedestal tilt - South	0.0	1.3	-37.5	3.1	0.0	4.4	-37.1	3.7
Canting	0.0	1.3	-38.1	1.7	0.0	5.0	-38.0	2.0
Heliostat positioning	16.9	0.2	0.0	0.0	16.9	0.1	-0.2	0.0
Temporal delay	-17.8	0.6	0.0	4.7	-18.3	0.1	-0.2	0.9

Table 4
Mean and standard deviation of the intrinsic drift shown in Fig. 3(a) and (b).

Winter solstice				Summer solstice			
μ_x (mrad)	σ_x (mrad)	μ_z (mrad)	σ_z (mrad)	μ_x (mrad)	σ_x (mrad)	μ_z (mrad)	σ_z (mrad)
0.000	0.210	0.052	0.002	0.000	0.133	-0.145	0.002

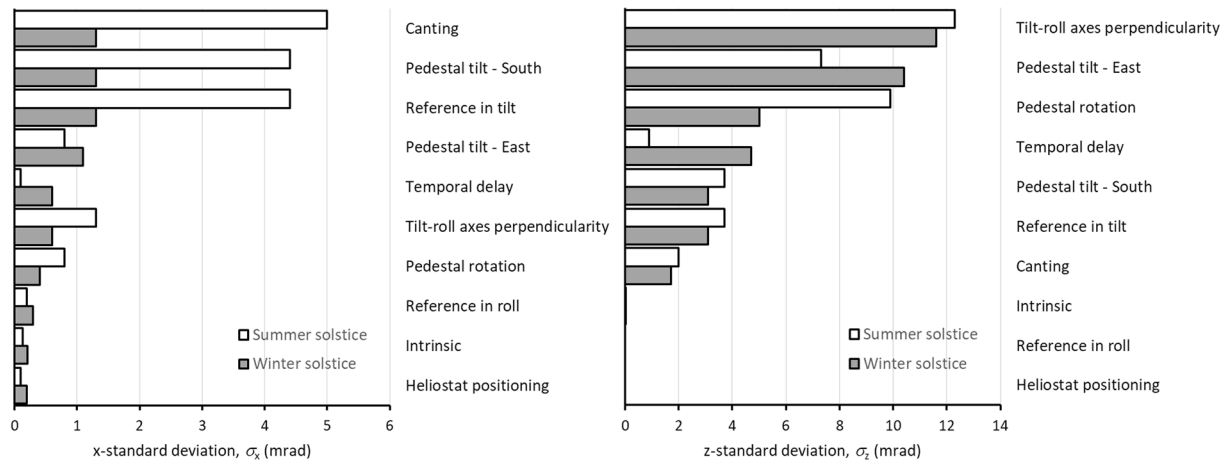


Fig. 13. Standard deviation of the drift curves obtained for an angular error of 20 mrad and those of the intrinsic drift. (Left) x-component in winter and summer solstices; (right) z-component in winter and summer solstices.

perpendicularity error (already centered), pedestal rotation, pedestal tilt towards the East/West, heliostat positioning error and temporal delay. However, this correction is not pertinent for the heliostat positioning error if the heliostat position changes in the north–south (Y) axis. If this happens, the reflected light will be deflected on the target towards the top or the bottom part, so the mean in the Z- direction will not be zero. Consequently, comparison between drift sources can be performed according to their standard deviation, since the first method allows centering all the drift curves without significantly altering their shape.

Fig. 13 shows the different standard deviations in X- and Z- directions sorted from the highest to the lowest. Comparison between x- and z-based standard deviations indicates that the latter are higher than the first ones. The differences are indeed as high as 12 times for the pedestal rotation error. Additionally, the x-standard deviation is highly dependent on sun position suffering important variations, which are as high as 3.9 times for canting error, between summer and winter solstice. These results point out that structure misalignments produce a solar spot displacement on the target due to drift that primary affect the vertical direction and presents the largest variation in the summer season.

The largest x-standard deviation corresponds to the canting error in summer solstice, and canting, pedestal tilt (south) and reference in tilt errors in winter solstice. Regarding to the z-component, the most crucial error is the tilt-roll axes perpendicularity for both winter and summer solstices, being followed by pedestal tilt (east) and rotation errors. The analysis underlines the relevance of structure able to provide a high-quality tilt-roll axes perpendicularity and accurate installation in order to achieve a well oriented tracking system.

6. Conclusions

Optimum performance of solar tower facilities requires a good understanding of all the phenomena involved in their operation. Hereof, a relevant effect occurring due to misalignments in the heliostats of the solar field is the drift, which results in a deviation of the focused solar beam with respect to the aiming point along the day. To correct this effect, all the misalignments producing it must be thoroughly investigated.

In this paper, several factors able to produce drift in tilt-roll tracking-

based heliostats have been investigated. Drift errors have been systematically studied and analyzed for this type of tracking system. With the aim to obtain the most detailed results, a Monte Carlo ray tracing method has been employed, in contrast to other studies where only the central ray was used. This approach has revealed the existence of an intrinsic drift, impossible to detect with the approximation of the central ray. This intrinsic drift can modify the drift curves produced by other factors, and is independent of the tracking system employed.

Even though the drift curves obtained here are only representative of the heliostat chosen, centered in the field and azimuthally aligned with the target, some of the results are general for tilt-roll tracking-based heliostats regardless the position of the heliostat in the field. For example, a reference error of the tilt and roll motor can always be corrected by applying an offset. Similarly, when the pedestal is tilted along the north–south axis, the resulting drift is identical to the drift corresponding to a reference error in the tilt motor (both errors have the same normal vector), and thus it can always be corrected by actuating over the tilt motor. Furthermore, for the perpendicularity error, the drift curve will always pass through the center of the target when the roll angle is zero. In the same way, if the facet has a canting error, the drift curves will be very similar to those corresponding to the reference error in tilt and pedestal tilt along the north–south axis for small roll angles.

As a noticeably result, it has been found that the most undesirable factors that produce drift are, for a heliostat centered in the field, the lack of perpendicularity between the tilt and roll axes, the rotation of the pedestal and the tilt of the pedestal along the east–west axis. All of them are associated with a large drift and the latter ones are both likely to occur when installing the heliostat in the solar field. Furthermore, these three errors cannot be corrected by just applying an offset.

Declaration of Competing Interest

The authors declared that there is no conflict of interest.

Acknowledgements

This project has received funding from the European Union’s Horizon 2020 research and innovation programme under grant agreement

No. 823802 (SFERA IID). The authors wish to thank to “Comunidad de Madrid” and European Structural Funds for their financial support to ACES2030-CM project (S2018/EMT-4319). AMH also acknowledges support from the Community of Madrid (Spain) through the Young Employment Program (PEJD-2017-PRE/AMB-4951).

References

- Batteiger, V., Brendelberger, S., Dufour, J., González, J., Iribarren, D., Koepf, E., Pitz-Paal, R., 2018. Sun-to-Liquid: Solar Fuels From H₂O, CO₂, and Concentrated Sunlight. 24th SolarPACES 2018 International Conference. AIP Publishing.
- Blanco-Muriel, M., Alarcón-Padilla, D.C., López-Moratalla, T., Lara-Coira, M., 2001. Computing the solar vector. *Sol. Energy* 70 (5), 431–441.
- Bonanos, A.M., 2012. Error analysis for concentrated solar collectors. *J. Renewable Sustainable Energy* 4 (6), 063125.
- Carretero, E., Preciado, J., Salinas, I., Ayora, I., Heras, C., 2019. Evaluation and measurement of heliostat misalignment in solar power plant using vector model. *Opt. Express* 27 (8), A257–A268.
- Chen, Y.T., Kribus, A., Lim, B.H., Lim, C.S., Chong, K.K., Karni, J., Blich, T.P., 2004. Comparison of two sun tracking methods in the application of a heliostat field. *J. Sol. Energy Eng.* 126 (1), 638–644.
- Chen, Y. T., Lim, B. H., & Lim, C. S. (2006). General sun tracking formula for heliostats with arbitrarily oriented axes.
- Chong, K.K., Wong, C.W., 2009. General formula for on-axis sun-tracking system and its application in improving tracking accuracy of solar collector. *Sol. Energy* 83 (3), 298–305.
- Collado, F.J., Gómez, A., Turégano, J.A., 1986. An analytic function for the flux density due to sunlight reflected from a heliostat. *Sol. Energy* 37 (3), 215–234.
- Díaz-Félix, L.A., Escobar-Toledo, M., Waissman, J., Pitalúa-Díaz, N., Arancibia-Bulnes, C. A., 2014. Evaluation of heliostat field global tracking error distributions by Monte Carlo simulations. *Energy Procedia* 49, 1308–1317.
- Escobar-Toledo, M., Arancibia-Bulnes, C.A., Iriarte-Cornejo, C., Waissman, J., Riveros-Rosas, D., Cabanillas, R.E., Estrada, C.A., 2014. Heliostat image drift behavior for different error sources. *J. Renewable Sustainable Energy* 6 (2), 023117.
- Gonzalo, I.B., Martínez-Hernández, A., Romero, M., González-Aguilar, J., 2020. Efficient Ray-Tracing Program to Simulate the Optical Performance of Heliostats in Concentrated Solar Power Facilities. Proceedings ISES Solar World Congress 2019.
- Guo, M., Wang, Z., Liang, W., Zhang, X., Zang, C., Lu, Z., Wei, X., 2010. Tracking formulas and strategies for a receiver oriented dual-axis tracking toroidal heliostat. *Sol. Energy* 84 (6), 939–947.
- Guo, M., Wang, Z., Zhang, J., Sun, F., Zhang, X., 2011. Accurate altitude–azimuth tracking angle formulas for a heliostat with mirror–pivot offset and other fixed geometrical errors. *Sol. Energy* 85 (5), 1091–1100.
- Guo, M., Sun, F., Wang, Z., Zhang, J., 2013a. Properties of a general azimuth–elevation tracking angle formula for a heliostat with a mirror-pivot offset and other angular errors. *Sol. Energy* 96, 159–167.
- Guo, M., Wang, Z., Sun, F., 2013b. Simulations of reflected sun beam traces over a target plane for an azimuth–elevation tracking heliostat with fixed geometric error sources. *Sol. Energy* 97, 102–111.
- Igel, E.A., Hughes, R.L., 1979. Optical analysis of solar facility heliostats. *Sol. Energy* 22 (3), 283–295.
- Iriarte-Cornejo, C., Arancibia-Bulnes, C.A., Salgado-Transito, I., Waissman, J., Cabanillas, R.E., Estrada, C.A., 2014. Compensation of heliostat drift by seasonal sampling. *Sol. Energy* 105, 330–340.
- Lara-Cerecedo, L. O., Moreno-Cruz, I., Pitalúa-Díaz, N., & Arancibia-Bulnes, C. A. (2016). Modeling of drift effects on solar tower concentrated flux distributions. *International Journal of Photoenergy*, 2016.
- Larmuth, J., Malan, K., & Gauché, P. (2013). Design and cost review of 2 m² heliostat prototypes. *Port Elizabeth*.
- Lipps, F.W., Vant-Hull, L.L., 1978. A cellwise method for the optimization of large central receiver systems. *Sol. Energy* 20 (6), 505–516.
- Mousazadeh, H., Keyhani, A., Javadi, A., Mobli, H., Abrinia, K., Sharifi, A., 2009. A review of principle and sun-tracking methods for maximizing solar systems output. *Renew. Sustain. Energy Rev.* 13 (8), 1800–1818.
- Romero, M., González-Aguilar, J., Luque, S., 2017. Ultra-modular 500m² heliostat field for high flux/high temperature solar-driven processes. *AIP Conf. Proc.* 1850, 030044.
- Romero, M., González-Aguilar, J. & Zarza, E. Concentrating solar thermal power. In *Energy efficiency and renewable energy handbook*, Chapter 42, edited by D. Y. Goswami, F. Kreith (ROUTLEDGE in association with GSE Research., Florida, USA, 2016), pp. 1237-1345.
- Romero, M., González-Aguilar, J., Sizmann, A., Batteiger, V., Steinfeld, A., Zoller, S., Liefstink, D., 2019. Solar-Driven Thermochemical Production of Sustainable Liquid Fuels from H₂O and CO₂ in a Heliostat Field. In: *Proceedings ISES Solar World Congress 2019*. Published by International Solar Energy Society (Open Access). <https://doi.org/10.18086/swc.2019.23.02>.
- Salomé, A., Chhel, F., Flamant, G., Ferrière, A., Thiery, F., 2013. Control of the flux distribution on a solar tower receiver using an optimized aiming point strategy: Application to THEMIS solar tower. *Sol. Energy* 94, 352–366.
- Schramek, P., Mills, D.R., 2004. Heliostats for maximum ground coverage. *Energy* 29 (5–6), 701–713.
- Stone, K.W., Jones, S.A., 1999. Analysis of solar two heliostat tracking error sources. Boeing Co., Huntington Beach, CA (US).
- Stone, K.W., June, 1998, *Open Loop Track Alignment Methodology*. Solar Engineering-1998, ASME.
- Torres-Roldán, M., López-Luque, R., Varo-Martínez, M., 2015. Design of an innovative and simplified polar heliostat for integration in buildings and urban environments. *Sol. Energy* 119, 159–168.
- Wendelin, T. (2003, March). SolTrace: a new optical modeling tool for concentrating solar optics. In *ASME 2003 International Solar Energy Conference* (pp. 253-260). American Society of Mechanical Engineers Digital Collection.
- Zaibel, R., Dagan, E., Karni, J., Ries, H., 1995. An astigmatic corrected target-aligned heliostat for high concentration. *Sol. Energy Mater. Sol. Cells* 37, 191–202.